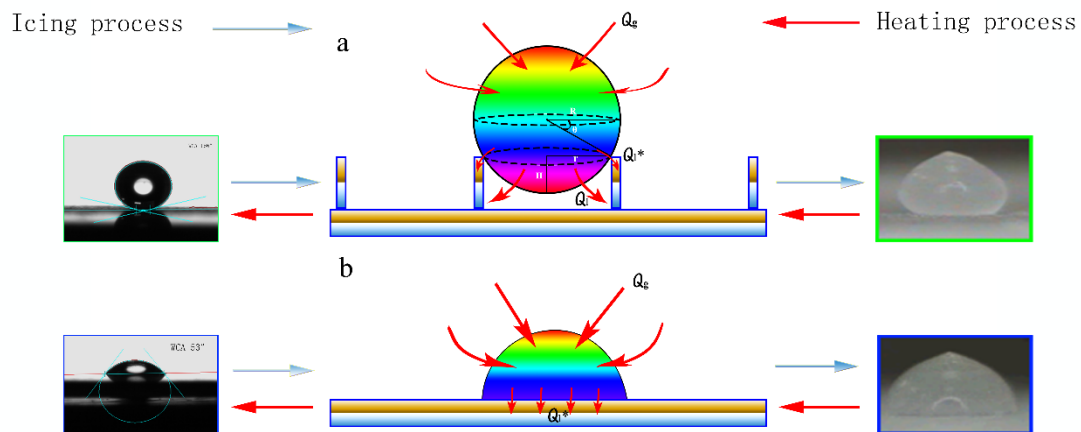


# Anti-icing property of bio-inspired micro-structure superhydrophobic surfaces and heat transfer model

Yan Liu<sup>a1</sup>, Xinlin Li<sup>a</sup>, Jingfu Jin<sup>b</sup>, Jiaan Liu<sup>c</sup>, Yuying Yan<sup>d</sup>, Zhiwu Han<sup>a</sup>, Luquan Ren<sup>a</sup>

a. Key Laboratory of Bionic Engineering (Ministry of Education), Jilin University, Changchun 130022, China; b. College of Biological and Agricultural Engineering, Jilin University, Changchun 130022, PR China; c. Key Laboratory of Automobile Materials (Ministry of Education) and College of Materials Science and Engineering, Jilin University, Changchun, 130022, P. R. China; d. Energy & Sustainability Research Division, Faculty of Engineering, University of Nottingham, UK

## Abstract



Ice accumulation is a thorny problem which may inflict serious damage even disasters in many areas, such as aircraft, power line maintenance, offshore oil platform and locators of ships. Recent researches have shed light on some promising bio-inspired anti-icing strategies to solve this problem. Inspired by typical plant surfaces with

17 super-hydrophobic character such as lotus leaves and rose petals,  
18 structured superhydrophobic surface are prepared to discuss the anti-icing  
19 property. 7075 Al alloy, an extensively used materials in aircrafts and  
20 marine vessels, is employed as the substrates. As-prepared surfaces are  
21 acquired by laser processing after being modified by stearic acid for 1h at  
22 room temperature. The surface morphology, chemical composition and  
23 wettability are characterized by means of SEM, XPS, Fourier transform  
24 infrared (FTIR) spectroscopy and contact angle measurements. The  
25 morphologies of structured as-prepared samples include round hump,  
26 square protuberance and mountain-range-like structure, and that the  
27 as-prepared structured surfaces shows an excellent superhydrophobic  
28 property with a WCA as high as  $166 \pm 2^\circ$ . Furthermore, the anti-icing  
29 property of as-prepared surfaces was tested by a self-established  
30 apparatus, and the crystallization process of a cooling water on the  
31 sample was recorded. More importantly, we introduced an model to  
32 analyze heat transfer process between the droplet and the structured  
33 surfaces. This study offers an insight into understanding the heat transfer  
34 process of the superhydrophobic surface, so as to further research about  
35 its unique property against ice accumulation.

36

37 **Key words:** Anti-icing, Superhydrophobic, Aluminum alloy, Laser  
38 process, Heat transfer

## 39 **1. Introduction**

40 Many researches for anti-/de-icing performance of the surfaces, such  
41 as aircrafts, wind turbines, power lines, marine vessels, highways,  
42 buildings, refrigeration equipment, and telecommunication equipment,  
43 have been made, because the formation of ice on these surfaces can cause  
44 many bad impacts.<sup>[1-3]</sup> Some of the disasters in the aviation, in particular,  
45 have been attributed to the accumulation of ice on the windward surface  
46 of aircrafts during a flight, for the aerodynamic forces are altered, either  
47 increasing drag or decreasing lift. In order to solve this problem, a  
48 particular attractive technique, ie. anti-icing performance of SHS  
49 (superhydrophobic surface), have been researched recently.<sup>[4-6]</sup>

50 Inspired by many plants and insects, such as lotus leaves<sup>[7]</sup>, rose  
51 petals<sup>[8]</sup>, legs of water striders<sup>[9]</sup> and butterfly wings<sup>[10]</sup>, wettability<sup>[11]</sup>,  
52 which is dominated by both the chemical composition and the  
53 morphology of the surface<sup>[12, 13]</sup>, is one of the unusual properties of these  
54 plants and insects. Abiding by the mechanism of the wettability<sup>[14, 15]</sup>, the  
55 fabrication of SHS involves two steps, the creation of a rough micro/nano  
56 scale structure and followed with the passivation of the rough surface by  
57 a low surface energy chemical reagents.<sup>[16, 17]</sup> By now, many studies have  
58 successfully fabricated the superhydrophobic surfaces with anti-icing  
59 property by various methods. Cao et al.<sup>[18]</sup> fabricated the  
60 superhydrophobic coatings with anti-icing property by using

61 nanoparticle-polymer composites successfully, which are able to prevent  
62 ice formation upon impact of supercooled water both in laboratory  
63 conditions and in naturally occurring environments, demonstrating that  
64 the particle sizes of the coatings are critical for anti-icing property. Guo et  
65 al.<sup>[19]</sup> systematically studied the anti-icing properties of different  
66 structured surfaces, i.e. micro/nano- structured surface (MN-surface),  
67 nanostructured surfaces (N-surfaces), micro-structured  
68 surfaces(M-surfaces), smooth surfaces without any structure (S-surfaces),  
69 finding that the MN-surface composed of microratchets combined with  
70 nano-hairs on a metal substrate shows an excellent icephobic/anti-icing  
71 property than others. Moreover, Kim et al.<sup>[20]</sup> employed a radically  
72 different method to fabricate a new type of ice-repellent material based on  
73 slippery, liquid-infused porous surfaces (SLIPS) on aluminum substrates,  
74 which is proved to have a promising and broad application for its robust  
75 anti-icing properties. Actually, most of researches have proved that  
76 morphology of the superhydrophobic surfaces is a very important factor  
77 for its anti-icing property.<sup>[5, 21-23]</sup> And experiments carried out on designed  
78 micro-/nanostructured superhydrophobic surfaces show a spontaneous  
79 and controllable removal of condensed microdroplets at high  
80 supersaturation via self-propelled jumping.<sup>[24-27]</sup> However, few researches  
81 thoroughly elaborate that how the surface morphology influence the heat  
82 transfer process.

83 In this paper, 7075 Al alloy is employed as the substrates of the SHS,  
84 which is widely applied in aviation, mechanical equipment, and mould  
85 processing, for its excellent property of high strength and mechanical  
86 capacity. [28, 29] We study the anti-icing property of SHS on 7075 Al alloy  
87 with different morphologies by laser processing, such as round hump,  
88 square protuberance and mountain-range-like structure. We demonstrated  
89 that the different morphology of the SHS exhibited relatively different  
90 anti-icing properties, tested by a robust apparatus established by ourselves,  
91 by which we decreased the temperature from the room temperature of  
92 16.0 °C to -15 °C at the rate of 0.2°C/s with the relative humidity of  
93 53±5%, and the icing time on these SHS can be postponed obviously  
94 compared to the bare 7075 Al alloy substrate. In order to investigate the  
95 anti-icing property in dynamic situations, a stream of water was sprayed  
96 on the experimental surfaces after they were tilted, controlling the  
97 temperature at -15 °C and the relative humidity of 53±5% stably.  
98 Interestingly, the water sprayed on the no structured surfaces iced up and  
99 accumulate gradually; while on the SHS flowed down immediately, only  
100 small parts of which covered with ice. We find that the anti-icing  
101 capability of the SHS, to some extent, is determined by the micro array  
102 structure of SHS. Furthermore, we present a model to analyze heat  
103 transfer process between the droplet and the structured surfaces.

## 104 **2. Experimental**

## 105 **2.1 Materials**

106 7075 Al alloy sheets (0.4wt% Si, 0.5wt% Fe, 2.0wt% Cu, 0.3wt% Mn,  
107 2.9wt% Mg, 0.28wt% Cr, 6.1wt% Zn, 0.2wt% Ti, with balance being Al)  
108 with the size of 20mm×20mm×1mm, emery paper No. 400, No. 800 and  
109 No. 1500, acetone, ethanol and stearic acid ( $\text{CH}_3(\text{CH}_2)_{16}\text{COOH}$ ) (99%,  
110 Tianjin East China Chemicals Co. Ltd.) were used for experiments  
111 reported in this paper.

## 112 **2.2 The experimental process**

113 7075 Al alloy sheets were polished with 500#, 800# and 1500#  
114 emery papers in turn, and then cleaned with acetone and ethanol in an  
115 ultrasonic bath for 10 min respectively. The samples with different  
116 morphology were irradiated by fiber laser for two times with the  
117 irradiated area of 10 mm×10 mm, the parameters employed of which: 50  
118 W average power, 20 kHz repetition rate, 200 ns pulse duration, 500  
119 mm/s scanning speed, after desirable patterns of the surface morphology  
120 were successfully designed by computer. Afterwards the samples were  
121 cleaned with acetone and ethanol in an ultrasonic bath for 15 min  
122 respectively. Finally, all of the samples were modified with the 0.01  
123 mol/L solution of stearic acid (SA) at ambient temperature for 60 min and  
124 dried in atmosphere condition.

## 125 **2.3 Characterization**

126 The surface morphologies was analyzed by scanning electron  
127 microscopy (SEM, EVO 18, ZEISS), and the surface composition was  
128 detected by X-ray photoelectron spectroscopy (XPS, SPECS XR50,  
129 Japan). The surface wetting behaviors is assessed by the water contact  
130 angle (CA) which is collected by a contact angle meter (JC2000A  
131 Powereach, China) with sessile drop method at ambient temperature of  
132  $23\pm 2$  °C and the relative humidity of  $53\pm 5\%$ . Water droplets with the  
133 volume of 3  $\mu$ L were carefully dropped onto the surfaces in five different  
134 positions to obtain the average static contact angle value. The infrared  
135 spectrum of the samples were recorded with a Fourier Transform-Infrared  
136 (FTIR, JACSCO, Japan) spectrometer at a resolution of 2  $\text{cm}^{-1}$ . FT-IR  
137 spectrum of the samples were obtained between 4,000 and 400  $\text{cm}^{-1}$  by an  
138 FT-IR spectrometer.

#### 139 **2.4 Anti-icing property**

140 An apparatus composed of temperature control system, image  
141 acquisition system and data collection system was established including a  
142 Recycled Water Temperature Controller (CMX-250-4/240-NM, OMEGA,  
143 America), (TES1310, ESM, China), data acquisition (DAQ11625,  
144 Quatronix, China), a CCD camera (73X11H, Mintron, China) and a  
145 computer etc. The schematic diagram of the apparatus is shown in Fig.1.  
146 Firstly, the sample was fixed with heat conductive silicone grease on the  
147 experimental plate horizontally at ambient temperature of  $16\pm 2$  °C and

148 the relative humidity of  $53\pm 5\%$ . And then the temperature of  
149 experimental plate, monitored by the digital temperature measuring  
150 instrument, was decreased from the room temperature of  $16.0\text{ }^{\circ}\text{C}$  to  
151  $-15\text{ }^{\circ}\text{C}$  at the rate of  $0.2^{\circ}\text{C/s}$  using the Recycled Water Temperature  
152 Controller, after the water droplets with the volume of  $5\text{ }\mu\text{L}$  were  
153 carefully dropped onto the surfaces with different morphology which  
154 were fixed on the experimental plate with heat conductive silicone grease,  
155 respectively. At the meantime, the icing process was monitored and  
156 collected by the CCD camera. Finally, the SHS of the samples,  
157 respectively, were tilted with an angle of  $5^{\circ}$  and fixed on the experimental  
158 plate with heat conductive silicone grease as well. When the temperature  
159 of the experimental plate was stable at  $-15\text{ }^{\circ}\text{C}$ , a steam of water was  
160 sprayed onto the as-prepared surfaces, and different liquid states were  
161 captured by camera.

## 162 **3. Results and discussion**

### 163 **3.1 Surface morphology**

164 Surface morphology is an important factor of super-hydrophobic  
165 properties, therefore, as-prepared surfaces were characterized by SEM.  
166 Fig. 2 shows the SEM images of the sample surfaces with different  
167 morphology. It can be found that micro scale structure was successfully  
168 obtained on 7075 Al alloy substrates, which was proved to play a major



169 role to the different properties of the surfaces. After laser processing, the  
170 target part of the surface was removed by high power laser beam, so that  
171 the regular morphology was formed as we designed. As shown in Fig.2a,  
172 an orderly matrix of regular round humps (R-surface) can be obviously  
173 observed in low magnification, as well as the gaps irradiated by laser  
174 beam. In high magnification, it is amazing to find the round hump is  
175 covered by nano-scale mastoid structure, as shown in Fig.2d, which can  
176 attribute to the deposition of SA film. It is easy to deposition on the sharp  
177 edge of each hump, and condensate gradually to form the nano-scale  
178 mastoid structure on it. This phenomenon is also found in the SEM image  
179 of the other two surfaces. In Fig.2b, SEM image of the morphology of the  
180 regular square protuberance (S-surface) was captured in low  
181 magnification. The distance of each two square protuberances are as same  
182 as the round humps` shown in Fig.2a, so that other interference factors  
183 except the morphology can be neglected. In the corresponding image,  
184 Fig.2e, is the high magnification image of the square protuberance, on  
185 which nano-scale mastoid structure is clearly found as well. As to Fig.2c,  
186 the image of an array of strips in low magnification are captured by the  
187 SEM, while a mountain range-like structure (M-surface) detected in high  
188 magnification, as shown in Fig.2f. More importantly, the micro array  
189 structure is more complex than the other two as-prepared surfaces. As a  
190 result, much more air can be trapped in the void, which is one of the most

191 important character contributing to the water repelling property of  
192 superhydrophobic surface.

### 193 **3.2 Chemical characterization**

194 In addition, FT-IR spectrum was employed to verify the chemical  
195 composition of the as-prepared surface modified by stearic acid. It can be  
196 seen in Fig.3. That many absorption bands are detected on as-prepared  
197 surfaces, compared with the typical FT-IR spectrum of stearic acid, which  
198 indicates that 7075 Al alloy aluminum alloy surface has been modified by  
199 stearic acid. An absorption peak is found at  $1701\text{ cm}^{-1}$  in the low region,  
200 corresponding to the free  $\text{-COO-}$  groups in the typical FT-IR ( $1702\text{ cm}^{-1}$ )  
201 spectrum. This can be attributed to double molecular association of the  
202 carboxylic acid molecule. In addition, another two adsorption peaks was  
203 found at approximately  $2920\text{ cm}^{-1}$  and  $2851\text{ cm}^{-1}$  in the high-frequency  
204 region respectively, which may be attributed to the  $\text{-CH}_2\text{-}$  asymmetric and  
205 symmetric stretching vibrations, while the typical FT-IR spectrum of  
206 stearic acid for  $\text{-CH}_2\text{-}$  is at  $2917\text{ cm}^{-1}$  and  $2849\text{ cm}^{-1}$ . Meanwhile, the peak  
207 at  $1430\text{ cm}^{-1}$  is ascribed to the vibration of the C-O group.

208 The presence of C, O and Al on the aluminum alloy surfaces modified  
209 by stearic acid was revealed by X-ray photoelectron spectroscopy (XPS)  
210 investigations, as shown in Fig.4. Fig.4a shows the full-spectrum of the  
211 as-prepared surfaces and three strong peaks of Al 2p, C 1s and O 1s were  
212 proved to increase significantly compared to the untreated 7075 Al alloy

213 surface, and Fig.2b presents the strong peak of C 1s is at 284.71 eV. In  
214 conclusion, as-prepared surfaces were modified by stearic acid  
215 successfully, i.e. the existence of C-H and COO- from stearic acid  
216 ( $\text{CH}_3(\text{CH}_2)_{16}\text{COOH}$ ) on aluminum alloy surfaces. Low energy materials  
217 with micro-structured films make the Cassie state more stable, which will  
218 help to amplify the hydrophobicity of the rough substrate. These results  
219 allowed us to hypothesize that the bonds between the SA molecules and  
220 the metal surface are formed through the condensation reaction, in which  
221 the carboxyl group (COO-H) combines with the aluminum hydroxyl  
222 group (Al-OH), releasing water and forming the aluminum carboxylate  
223 bond COO-Al:[30-32]



### 225 **3.3 Wettability**

226 The topographical structure and the chemical compositions are two  
227 important factors determined the wettability of the solid material.[33-36] As  
228 we mention above, all of the as-prepared superhydrophobic surfaces were  
229 successfully covered with a film of SA molecules. Once morphology of  
230 as-prepared surfaces changed from smooth to a topological rough  
231 structure, the wettability of the surfaces transformed from a hydrophilic  
232 character to a superhydrophobic state. Fig.5 shows the water contact  
233 angle (WCA) of the as-prepared surfaces with different morphology, bare  
234 surface(B), square protuberance structure (S), round hump structure (R)

235 and mountain range-like structure (M), modified by stearic acid. The bare  
236 surface without any structure and SA coating exhibits the hydrophility  
237 with contact angle of  $53^\circ$ . The surface of mountain range-like structure  
238 shows an excellent superhydrophobicity, and the WCA reached  $166\pm 2^\circ$ .  
239 Although the WCA of the other two surfaces, surface of square  
240 protuberance structure and surface of round hump structure, are not as  
241 high as the surface of mountain range-like structure, they are shown the  
242 superhydrophobic property as well, reaching  $157\pm 2.8^\circ$  and  $161\pm 2.2^\circ$ . As  
243 proved by many researches, the morphology of the surface is an  
244 indispensable factor to superhydrophobic property, thus the optimum  
245 micro-structure of the surface is made, the better superhydrophobic  
246 surface is obtained. The insets of Fig.5 systematically illustrates the state  
247 of as-prepared surfaces, labelled as INS.a, b and c respectively. INS.a  
248 shows the model of water droplet on bare surface, which can be  
249 recognized as Wenzel state. At this state, the wet contact (i.e., whole  
250 contact) between solid-liquid interfaces, so the existed continuous  
251 three-phase contact line leads to high adhesion of the surface, for which  
252 drop can hardly rolls off the surface. INS.b and c are models of the other  
253 three as-prepared superhydrophobic surfaces, which can be recognized as  
254 Cassie-Baxter state. Compared with the bare surface, the droplets are of  
255 composite contact on solid-liquid interfaces, so the discontinuous  
256 three-phase contact line exists and leads to low adhesion of the surface,

257 for which drop easily rolls off the surface. More importantly, with so  
258 much trapped-air between the droplets and surfaces, the droplet is  
259 completely suspended over the surfaces, which contributes the different  
260 wettability of the surfaces. However, the triple-phase contact line of  
261 different superhydrophobic surfaces is not identical. Superhydrophobic  
262 surfaces with square protuberance structure and round hump structure (as  
263 shown in the INS.b) have larger contact area than surfaces with mountain  
264 range-like structure (as shown in INS.c), so this could attribute to the  
265 difference of icing time.

### 266 **3.4 Anti-icing properties**

267 Superhydrophobic surfaces, as a passive anti-icing surfaces, has  
268 shown a promising future in the industrial applications, and great efforts  
269 have been made to invent new patent of these material with anti-icing and  
270 deicing capacities and study the mechanism.<sup>[6, 37]</sup> Because of the existence  
271 of vapor pockets at the solid-liquid interface in the Cassie-Baxter state<sup>[38]</sup>,  
272 water droplet can be suspended over the superhydrophobic surfaces and  
273 easily roll off. The delayed freezing time of water droplet on the  
274 superhydrophobic surface is another important indicator for the anti-icing  
275 property.<sup>[39-42]</sup> As discussed above, the as-prepared structured surface  
276 shows various wetting properties, which may really affect anti-icing  
277 properties under low temperature conditions. Fig.6 (1)a, b, c and d show  
278 the real-time status of water droplet in the volume of 5  $\mu$ L on the

279 as-prepared surface of mountain range-like structure (M), square  
280 protuberance structure (S), round hump structure (R) and bare surface(B)  
281 respectively. Initially, the reference drops on all surfaces are transparent.  
282 When the temperature of the experimental plate is decreased gradually,  
283 the drop on the B-surface becomes non-transparent at first after 319s,  
284 which indicates the drop is becoming frozen. However, the shape of the  
285 drops is changed after 325s, indicating the drop is frozen totally.  
286 Observed in turn, the drop on the R-surface and S-surface becomes  
287 non-transparent after 1146 s and 1160s respectively, and frozen after  
288 1153s and 1165s respectively with shape being changed. Obviously, the  
289 drop on the M-surface then becomes non-transparent after 1933s, and is  
290 frozen after 1938s, indicating this surface has a relatively long time to  
291 resist the water freezing. To further illustrate the icing process, Fig. 6e  
292 shows the icing mechanism of water droplet on as-prepared  
293 superhydrophobic surfaces. As the temperature of experimental plate  
294 decreased and stably kept at  $-15^{\circ}\text{C}$  with the relative humidity of  $53\pm 5\%$ ,  
295 the Cassie–Baxter state still existed on the superhydrophobic surfaces.  
296 But when delay time is at 1146s, droplet on R-surfaces became non  
297 transparent firstly, and shape of the droplet was changed to peach-like at  
298 1154s. At that time, Cassie–Baxter state missed and droplet was not  
299 suspended at all. However, when the temperature of the experimental  
300 plate return to ambient temperature, the SHS recovered to Cassie–Baxter

301 state, and droplet return to be suspended as well. All superhydrophobic  
302 surfaces mentioned above share with the same mechanism. As to  
303 B-surface, droplets exist as hemisphere, which can be described as  
304 Wenzel state<sup>[43]</sup>.

305       Consequently, delayed freezing time is roughly recorded by observing  
306 the non-transparency of the drop at -15 °C, as shown in Fig.6(2). The  
307 icing time on these SHS can be postponed from 325s to 1938s compared  
308 to the normal aluminum alloy surface. This implies that the differences of  
309 the micro-structure of SHS can significantly impact delayed freezing time.  
310 When the temperature of as-prepared surface was heated to room  
311 temperature, the droplet returns to be suspended upwards and the  
312 discontinuous three-phase contact line between the droplet and surface is  
313 basically recovered, which is slightly similar to the original contact state.

314       The temperature-induced pinning transition of droplets observed for  
315 the SHS at -15 °C can be explained using a model which analyzes droplet  
316 heat transfer process at the interface between the droplet and the  
317 micro-structure, as illustrated by Fig.6(3)a. Considering the droplet is  
318 suspended over the surfaces and the solid–liquid–air three-phase  
319 interfaces exists, there are two approaches to gain or lose heat, i.e. it gains  
320 heat from air in forms of contact heat conduction and thermal radiation  
321 and it loses heat to the cold surface through contact heat conduction and  
322 thermal radiation between the drop and the micro-structure. But what we

323 focus on is the process of icing, so we leave out the heat gain by  
324 micro-structure for the temperature of experimental plate is lower than  
325 that of droplet.

326 The relationship between heat gain and loss is expressed as:<sup>[44]</sup>

$$327 \quad Q_d = Q_g - Q_l - Q_l^*$$

328 Where  $Q_d$  is the heat quantity of droplet in unit time;  $Q_g$  is the heat  
329 quantity gains through thermal radiation in unit time;  $Q_l$  and  $Q_l^*$  is heat  
330 quantity loses through thermal radiation and heat transfer in unit time.

331 To further explain the mechanism of heat transfer on SHS, we  
332 introduce the area formula of the sphere and the equation of thermal  
333 radiation, but some hypotheses have to be made:

- 334 (1) The shape of droplet is never changed but a ball;  
335 (2) The thermal radiation between the droplet and air is homogeneous;

336 The equations involved present as follows:

337 Equation of irregular sphere surface area;

$$338 \quad S_d = 2\pi R^2(1 - \sin \theta) \quad (1)$$

339 Where  $S_d$  is the surface area of sphere;  $R$  is the radius of sphere;  $\theta$  is  
340 the spherical center angle;

341 The heat transfer through conduction between the interface of the  
342 water droplet and the coating surface can be described as the following  
343 equation:<sup>[45]</sup>

$$344 \quad Q = \alpha S_d (T_A - T_d) \quad (2)$$



345 Where  $Q$  is the heat quantity in unit time;  $\alpha$  is radiant heat-transfer  
 346 coefficient(according to different materials);  $T_A$  is the temperature of  
 347 ambient temperature;  $T_d$  is the temperature of sphere.

348 Referring to the equations mentioned above, we put forward an  
 349 equation of heat gain and loss:

$$350 \quad \begin{aligned} Q_d &= \alpha S_g (T_A - T_d) - \alpha S_l (T_A^\lambda - T_d) - Q_l^* \\ &= \alpha \cdot 2\pi R^2 (1 + \sin \beta) (T_A - T_d) - \alpha \cdot 2\pi R^2 (1 - \sin \beta) (T_A^\lambda - T_d) - Q_l^* \end{aligned}$$

351 Where  $S_g$  is the heat gain surface area of sphere;  $S_l$  is the heat loss  
 352 surface area of sphere;  $T_A^\lambda$  is temperature of the air between droplet and  
 353 experimental plate;  $\beta$  is contact angle of droplet (CA).

354 What we can learn in the equation is, there are two approaches to  
 355 keep the heat quantity of droplet in unit time  $Q_d$ , increasing the contact  
 356 angle of droplet and decreasing the heat quantity loses through heat  
 357 transfer. That means the bigger CA is, the more air trapped under the  
 358 droplet, so as to the less loss of heat quantity. Thus, this can well explain  
 359 the difference of delayed freezing times to the as-prepared  
 360 superhydrophobic surfaces. For example, the large contact angle of  
 361 M-surface contributes to more air trapped under the droplet, and less  
 362 liquid–solid contact area on the surface. As to the B-surface, there is no  
 363 trapped-air under the droplet and large liquid–solid contact area (as  
 364 shown in Fig. 6(3)b), so the equation of heat gain and loss can be  
 365 expressed as follows:<sup>[44]</sup>

$$366 \quad Q_d = Q_g - Q_l^*$$

367 Obviously, heat loss in unit time through heat transfer of liquid-solid  
368 interface is larger than heat gain in unit time through thermal radiation.  
369 Consequently, the heat quality of droplet decreases soon, leading to short  
370 delayed freezing times.

371 For further tests to the anti-icing property of as-prepared surfaces,  
372 with the relative humidity of  $53\pm 5\%$ , a stream of water was sprayed onto  
373 the B-, R-, S- and M-surfaces with an angle of  $5^\circ$ , respectively, the  
374 temperature of which was controlled at  $-15^\circ\text{C}$  stably, for 5 min in a  
375 permanent speed. Final result of the test is shown in Fig.7. In Fig.7a, the  
376 iced area was separated by red lines on S-surface. Almost 40% of the  
377 experimental area separated by blue square was covered with a thin film  
378 of ice, while most of the experimental area still exhibits ice-free  
379 properties. As to R-surface (Fig.9b), there are some droplets, separated by  
380 red circles, sticking on the experimental area, 30% of which was covered  
381 by a big block of ice separated by red lines. Obviously, M-surfaces  
382 (Fig.7c) shows the best anti-icing property, on which only some droplets  
383 stuck within experimental area, a large block of ice, however, was found  
384 on the non-experimental area. Moreover, in contrast to SHS, a strip of ice  
385 was clearly found on B-surface separated by red lines, shown in Fig.7d.  
386 As we discussed above, SHS exhibit an excellent water-repelling property  
387 at ambient temperature, as well as low adhesion. However, the situation is  
388 different, as the temperature decrease to  $-15^\circ\text{C}$ . To well illustrate this

389 phenomenon, we establish a model of icing process to schematically  
390 illustrate the mechanism of dynamic situation, as shown in Fig.8. It has  
391 been proved that droplets can be suspended over the SHS, resulting from  
392 the existence of trapped-air in the micro-structure and low-surface-energy  
393 material on the surface. However, the micro water droplets are easy to  
394 condensate in the gaps on the surface of micro-structure at low  
395 temperature.<sup>[46]</sup> In addition, some discrete frozen micro-drops first  
396 appeared on the superhydrophobic surfaces, and the following icing  
397 mainly occurred on these microcrystals and then expanded around them  
398 until covering the entire surface.<sup>[47]</sup> As a result, the Cassie–Baxter state  
399 disappears gradually, for most of the place used to trap air is taken up by  
400 condensate water. With the temperature of experimental plate decreased  
401 further, the surfaces adhesion strength increased dramatically.<sup>[48, 49]</sup> Once  
402 the strength is larger than Van Der Waals force existing between the water  
403 molecules, the bottom layer of water could be peeled off and left on the  
404 surface other than flow down, even though the up layer is still flowing.  
405 Finally, ice accumulation occurs on the superhydrophobic surfaces.

## 406 **Conclusions**

407 In summary, we have studied the anti-icing property of three  
408 different superhydrophobic surfaces, based on substrates of 7075 Al alloy,  
409 with different morphology, i.e. round hump, square protuberance and  
410 mountain-range-like structure, prepared by laser processing. Firstly, the

411 wettability of the as-prepared surfaces have been studied at ambient  
412 temperature with the relative humidity of  $53 \pm 5\%$ , and the SHS of  
413 mountain-range-like structure shows the best superhydrophobic property  
414 with a contact angle of  $166 \pm 2^\circ$ . Furthermore, systematic investigations  
415 of the static and dynamic freezing process show that the anti-icing  
416 capability is significantly impacted by the micro-structure of these  
417 superhydrophobic surfaces. Compared with the bare 7075 Al alloy, the  
418 SHS of mountain-range-like structure owns the longest delay time of  
419 1938s in static situation and the best ice-free property in dynamic  
420 situation. More importantly, we introduced a model to analyze heat  
421 transfer process between the droplet and the structured surfaces. This  
422 study offers an insight into understanding the heat transfer process of the  
423 superhydrophobic surface, so as to further research about its unique  
424 property against ice accumulation.

#### 425 **ACKNOWLEDGEMENTS**

426 The authors thank the National Natural Science Foundation of China  
427 (Nos. 51275555, 51475200 and 51325501), Science and Technology  
428 Development Project of Jilin Province (No.20150519007JH) and 111  
429 project (B16020) of China.

#### 430 **References**

- 431 [1] J.L. Laforte, M.A. Allaire, J. Laflamme, State-of-the-art on power line de-icing,  
432 Atmos. Res., 46 (1998) 143-158.  
433 [2] O. Parent, A. Ilinca, Anti-icing and de-icing techniques for wind turbines: Critical  
434 review, Cold Reg. Sci. Technol., 65 (2011) 88-96.

435 [3] S.A. Kulinich, M. Farzaneh, Ice adhesion on super-hydrophobic surfaces, Appl.  
436 Surf. Sci., 255 (2009) 8153-8157.

437 [4] Z. Zuo, R. Liao, C. Guo, Y. Yuan, X. Zhao, A. Zhuang, Y. Zhang, Fabrication and  
438 anti-icing property of coral-like superhydrophobic aluminum surface, Appl. Surf. Sci.,  
439 331 (2015) 132-139.

440 [5] M. Jung, T. Kim, H. Kim, R. Shin, J. Lee, J. Lee, J. Lee, S. Kang, Design and  
441 fabrication of a large-area superhydrophobic metal surface with anti-icing properties  
442 engineered using a top-down approach, Appl. Surf. Sci., 351 (2015) 920-926.

443 [6] J. Lv, Y. Song, L. Jiang, J. Wang, Bio-inspired strategies for anti-icing, ACS nano,  
444 8 (2014) 3152-3169.

445 [7] S.A. Kulinich, M. Farzaneh, How wetting hysteresis influences ice adhesion  
446 strength on superhydrophobic surfaces, Langmuir, 25 (2009) 8854-8856.

447 [8] L. Feng, Y. Zhang, J. Xi, Y. Zhu, N. Wang, F. Xia, L. Jiang, Petal Effect: A  
448 Superhydrophobic State with High Adhesive Force, Langmuir, 24 (2008) 4114-4119.

449 [9] X.-Q. Feng, X. Gao, Z. Wu, L. Jiang, Q.-S. Zheng, Superior Water Repellency of  
450 Water Strider Legs with Hierarchical Structures: Experiments and Analysis,  
451 Langmuir, 23 (2007) 4892-4896.

452 [10] Y. Zheng, X. Gao, L. Jiang, Directional adhesion of superhydrophobic butterfly  
453 wings, Soft Matter, 3 (2007) 178-182.

454 [11] T. Sun, L. Feng, X. Gao, L. Jiang, Bioinspired Surfaces with Special Wettability,  
455 Accounts Chem. Res., 38 (2005) 644-652.

456 [12] N. Gao, Y.Y. Yan, X.Y. Chen, X.F. Zheng, Superhydrophobic Composite Films  
457 Based on THS and Nanoparticles, J. Bionic Eng., 7 (2010) S59-S66.

458 [13] H.A. Stone, Ice-Phobic Surfaces That Are Wet, ACS Nano, 6 (2012) 6536-6540.

459 [14] C. Dorrer, J. R uhe, Some thoughts on superhydrophobic wetting, Soft Matter, 5  
460 (2009) 51-61.

461 [15] A. Marmur, Wetting on Hydrophobic Rough Surfaces: To Be Heterogeneous or  
462 Not To Be?, Langmuir, 19 (2003) 8343-8348.

463 [16] Y. Liu, Y. Bai, J. Jin, L. Tian, Z. Han, L. Ren, Facile fabrication of biomimetic  
464 superhydrophobic surface with anti-frosting on stainless steel substrate, Appl. Surf.  
465 Sci., 355 (2015) 1238-1244.

466 [17] D.K. Sarkar, M. Farzaneh, R.W. Paynter, Wetting and superhydrophobic  
467 properties of PECVD grown hydrocarbon and fluorinated-hydrocarbon coatings,  
468 Appl. Surf. Sci., 256 (2010) 3698-3701.

469 [18] L. Cao, A.K. Jones, V.K. Sikka, J. Wu, D. Gao, Anti-icing superhydrophobic  
470 coatings, Langmuir, 25 (2009) 12444-12448.

471 [19] P. Guo, Y. Zheng, M. Wen, C. Song, Y. Lin, L. Jiang, Icephobic/anti-icing  
472 properties of micro/nanostructured surfaces, Adv. Mater., 24 (2012) 2642-2648.

473 [20] P. Kim, T.-S. Wong, J. Alvarenga, M.J. Kreder, W.E. Adorno-Martinez, J.  
474 Aizenberg, Liquid-Infused Nanostructured Surfaces with Extreme Anti-Ice and  
475 Anti-Frost Performance, ACS Nano, 6 (2012) 6569-6577.

476 [21] J.D. Brassard, D.K. Sarkar, J. Perron, Synthesis of monodisperse fluorinated  
477 silica nanoparticles and their superhydrophobic thin films, ACS Appl. Mater.  
478 Interfaces, 3 (2011) 3583-3588.

479 [22] N. Purenkiy, J. Chanda, G. Stoychev, A. Synytska, L. Ionov, Anti-Icing  
480 Superhydrophobic Surfaces Based on Core-Shell Fossil Particles, *Adv. Mater.*  
481 *Interfaces*, 2 (2015) n/a-n/a.

482 [23] M. Zou, S. Beckford, R. Wei, C. Ellis, G. Hatton, M.A. Miller, Effects of surface  
483 roughness and energy on ice adhesion strength, *Appl. Surf. Sci.*, 257 (2011)  
484 3786-3792.

485 [24] J. Liu, H. Guo, B. Zhang, S. Qiao, M. Shao, X. Zhang, X.Q. Feng, Q. Li, Y.  
486 Song, L. Jiang, J. Wang, Guided Self-Propelled Leaping of Droplets on a  
487 Micro-Anisotropic Superhydrophobic Surface, *Angew. Chem. Int. Ed. Engl.*, 55  
488 (2016) 4265-4269.

489 [25] K. Rykaczewski, J.H.J. Scott, S. Rajauria, J. Chinn, A.M. Chinn, W. Jones, Three  
490 dimensional aspects of droplet coalescence during dropwise condensation on  
491 superhydrophobic surfaces, *Soft Matter*, 7 (2011) 8749-8752.

492 [26] M. He, X. Zhou, X. Zeng, D. Cui, Q. Zhang, J. Chen, H. Li, J. Wang, Z. Cao, Y.  
493 Song, L. Jiang, Hierarchically structured porous aluminum surfaces for high-efficient  
494 removal of condensed water, *Soft Matter*, 8 (2012) 6680.

495 [27] Q. Zhang, M. He, J. Chen, J. Wang, Y. Song, L. Jiang, Anti-icing surfaces based  
496 on enhanced self-propelled jumping of condensed water microdroplets, *Chem.*  
497 *Commun.*, 49 (2013) 4516-4518.

498 [28] S.W. Kim, D.Y. Kim, W.G. Kim, K.D. Woo, The study on characteristics of heat  
499 treatment of the direct squeeze cast 7075 wrought Al alloy, *Mater. Sci. Eng. A*,  
500 304–306 (2001) 721-726.

501 [29] R.K. Bhushan, S. Kumar, S. Das, Effect of machining parameters on surface  
502 roughness and tool wear for 7075 Al alloy SiC composite, *Int. J. Adv. Manuf.*  
503 *Technol.*, 50 (2010) 459-469.

504 [30] S.A. Kulinich, M. Honda, A.L. Zhu, A.G. Rozhin, X.W. Du, The icephobic  
505 performance of alkyl-grafted aluminum surfaces, *Soft Matter*, 11 (2015) 856-861.

506 [31] X. Yao, Q. Chen, L. Xu, Q. Li, Y. Song, X. Gao, D. Quéré, L. Jiang, Bioinspired  
507 Ribbed Nanoneedles with Robust Superhydrophobicity, *Adv. Funct. Mater.*, 20 (2010)  
508 656-662.

509 [32] B. Somlo, V. Gupta, A hydrophobic self-assembled monolayer with improved  
510 adhesion to aluminum for deicing application, *Mech. Mater.*, 33 (2001) 471-480.

511 [33] J. Zhang, Y. Han, A Topography/Chemical Composition Gradient Polystyrene  
512 Surface: Toward the Investigation of the Relationship between Surface Wettability  
513 and Surface Structure and Chemical Composition, *Langmuir*, 24 (2008) 796-801.

514 [34] N. Takeshita, L.A. Paradis, D. Öner, T.J. McCarthy, W. Chen, Simultaneous  
515 Tailoring of Surface Topography and Chemical Structure for Controlled Wettability,  
516 *Langmuir*, 20 (2004) 8131-8136.

517 [35] Q. Fu, G.V. Rama Rao, S.B. Basame, D.J. Keller, K. Artyushkova, J.E. Fulghum,  
518 G.P. López, Reversible Control of Free Energy and Topography of Nanostructured  
519 Surfaces, *J. Am. Chem. Soc.*, 126 (2004) 8904-8905.

520 [36] D. Öner, T.J. McCarthy, Ultrahydrophobic Surfaces. Effects of Topography  
521 Length Scales on Wettability, *Langmuir*, 16 (2000) 7777-7782.

522 [37] M.J. Kreder, J. Alvarenga, P. Kim, J. Aizenberg, Design of anti-icing surfaces:  
523 smooth, textured or slippery?, *Nat. Rev. Mater.*, 1 (2016) 15003.

524 [38] A. Cassie, S. Baxter, Wettability of porous surfaces, *Trans. Faraday Soc.*, 40  
525 (1944) 546-551.

526 [39] G. Heydari, E. Thormann, M. Järn, E. Tyrode, P.M. Claesson, Hydrophobic  
527 Surfaces: Topography Effects on Wetting by Supercooled Water and Freezing Delay,  
528 *J. Phys. Chem. C*, 117 (2013) 21752-21762.

529 [40] J. Hu, K. Xu, Y. Wu, B. Lan, X. Jiang, L. Shu, The freezing process of  
530 continuously sprayed water droplets on the superhydrophobic silicone acrylate resin  
531 coating surface, *Appl. Surf. Sci.*, 317 (2014) 534-544.

532 [41] F. Arianpour, M. Farzaneh, S.A. Kulinich, Hydrophobic and ice-retarding  
533 properties of doped silicone rubber coatings, *Appl. Surf. Sci.*, 265 (2013) 546-552.

534 [42] L. Boinovich, A.M. Emelyanenko, V.V. Korolev, A.S. Pashinin, Effect of  
535 wettability on sessile drop freezing: when superhydrophobicity stimulates an extreme  
536 freezing delay, *Langmuir*, 30 (2014) 1659-1668.

537 [43] R.N. Wenzel, Resistance of solid surfaces to wetting by water, *Ind. Eng. Chem.*,  
538 28 (1936) 988-994.

539 [44] X. Zhan, Y. Yan, Q. Zhang, F. Chen, A novel superhydrophobic hybrid  
540 nanocomposite material prepared by surface-initiated AGET ATRP and its anti-icing  
541 properties, *J. Mater. Chem. A*, 2 (2014) 9390-9399.

542 [45] Y. Tang, Q. Zhang, X. Zhan, F. Chen, Superhydrophobic and anti-icing properties  
543 at overcooled temperature of a fluorinated hybrid surface prepared via a sol-gel  
544 process, *Soft Matter*, 11 (2015) 4540-4550.

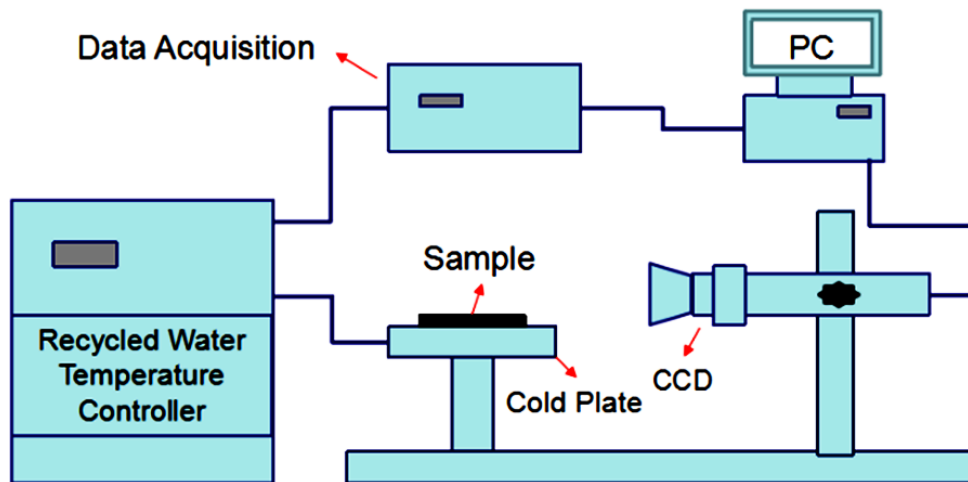
545 [46] M. Wen, L. Wang, M. Zhang, L. Jiang, Y. Zheng, Antifogging and icing-delay  
546 properties of composite micro- and nanostructured surfaces, *ACS Appl. Mater.*  
547 *Interfaces*, 6 (2014) 3963-3968.

548 [47] Q. Hao, Y. Pang, Y. Zhao, J. Zhang, J. Feng, S. Yao, Mechanism of delayed frost  
549 growth on superhydrophobic surfaces with jumping condensates: more than interdrop  
550 freezing, *Langmuir*, 30 (2014) 15416-15422.

551 [48] S.A. Kulinich, M. Farzaneh, On ice-releasing properties of rough hydrophobic  
552 coatings, *Cold Reg. Sci. Technol.*, 65 (2011) 60-64.

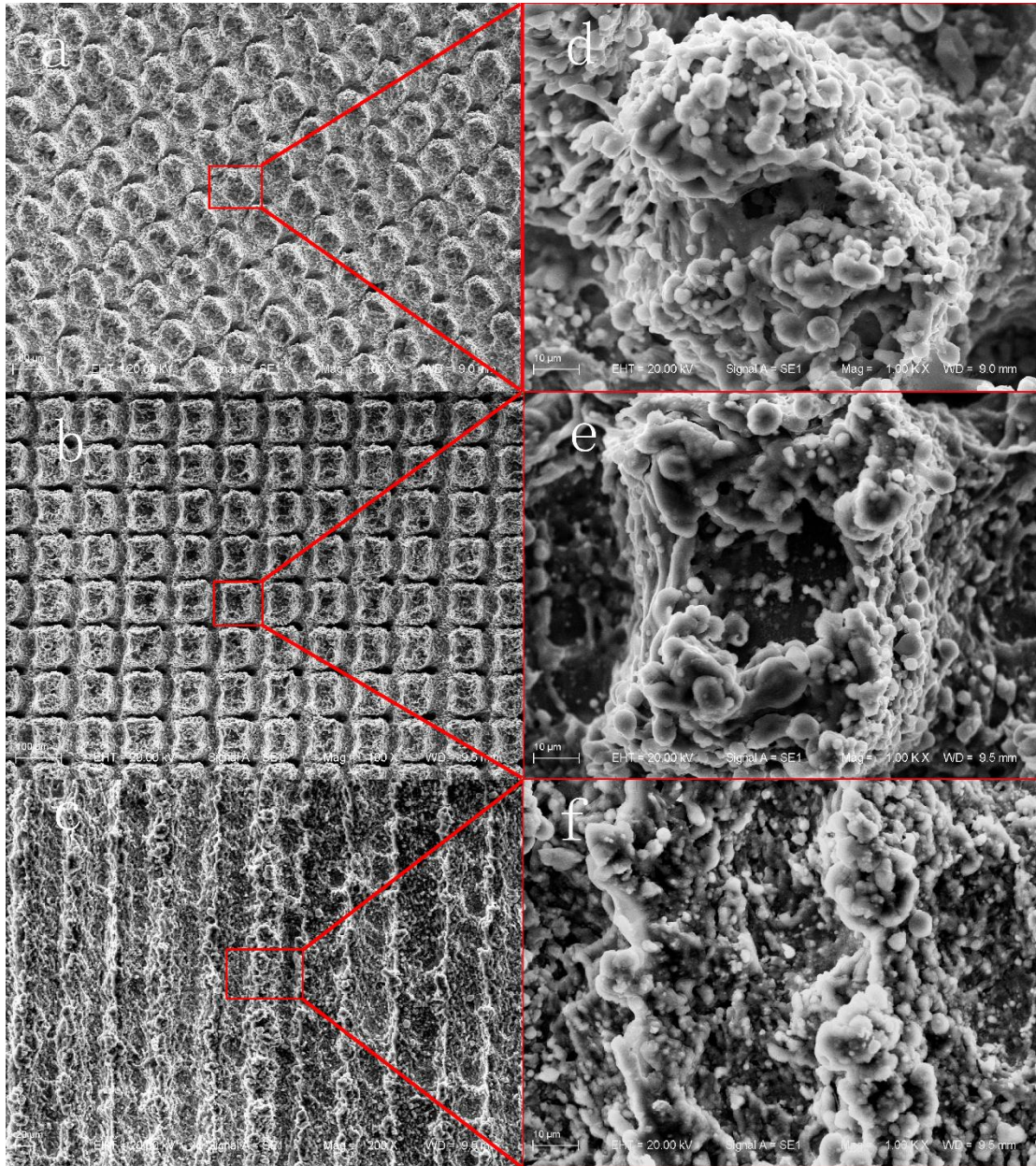
553 [49] L.B. Boinovich, A.M. Emelyanenko, Anti-icing Potential of Superhydrophobic  
554 Coatings, *Mendeleev Commun.*, 23 (2013) 3-10.

555



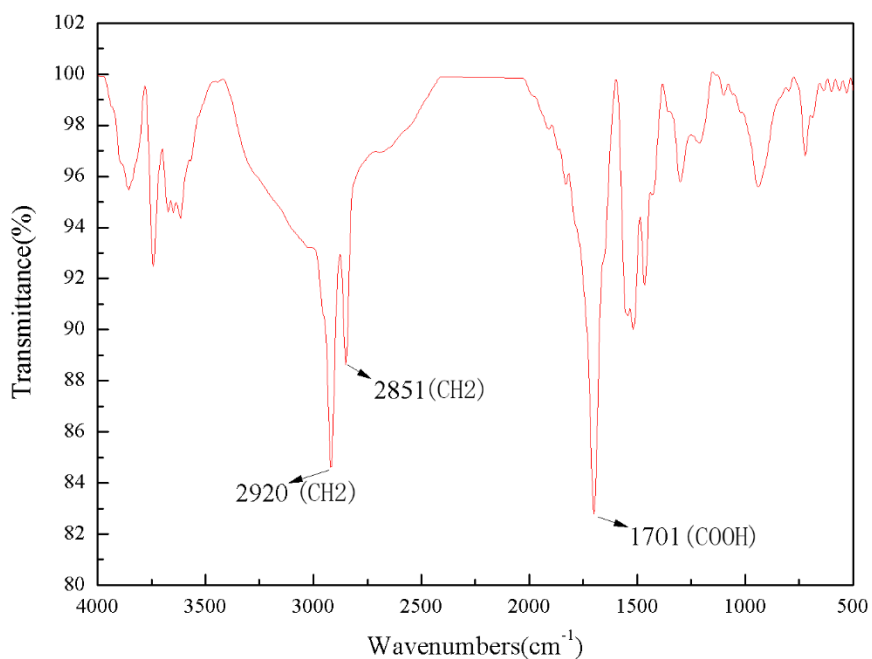
558 **Fig.1** The schematic representation of the experimental setup.





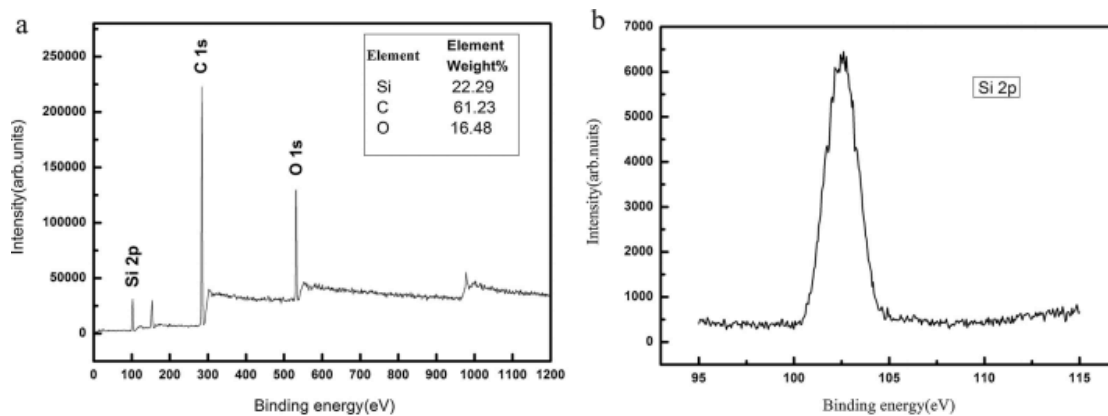
559

560 **Fig.2** SEM images of the sample surfaces with different morphology: (a)  
 561 Surface with the morphology of the regular round humps(R-surface), (b)  
 562 Surface with morphology of the regular square protuberance(S-surface),  
 563 (c) Surface with the morphology of mountain range-like structure  
 564 (M-surface), (d-f) high magnification SEM image of the corresponding  
 565 structured surfaces, respectively.



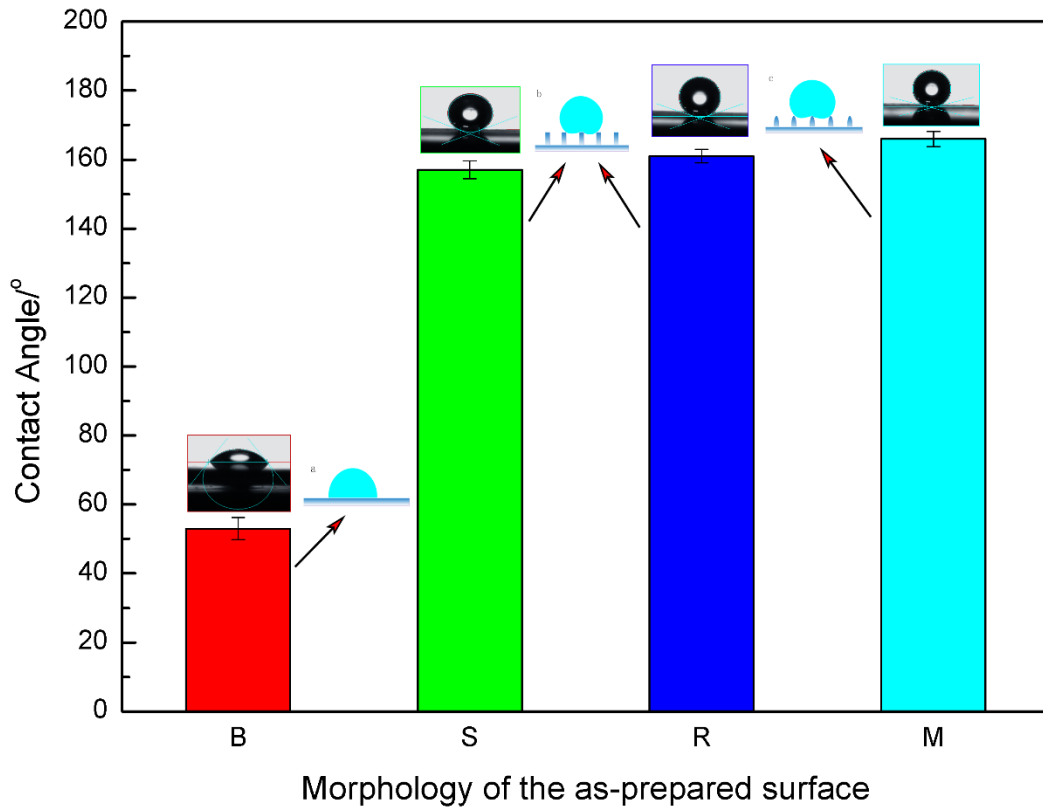
566

567 **Fig.3 FT-IR spectrum** of the Aluminum alloy surfaces modified by stearic  
 568 acid.



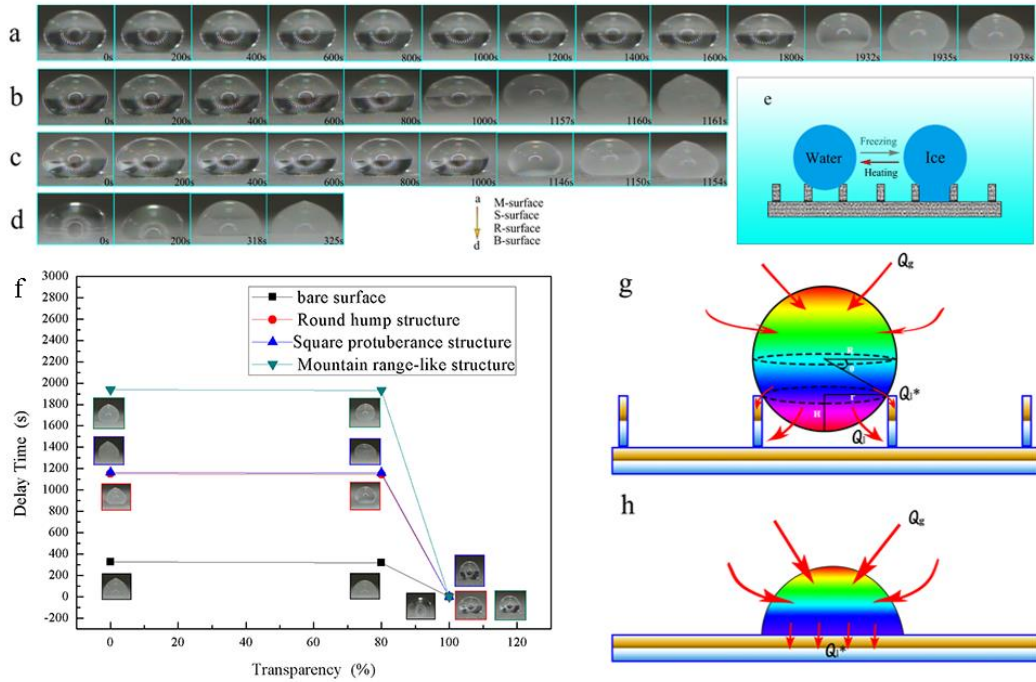
569

570 **Fig.4 XPS spectra** of the as-prepared superhydrophobic aluminum alloy  
 571 surface of (a) full-spectrum and (b) C 1s.



572

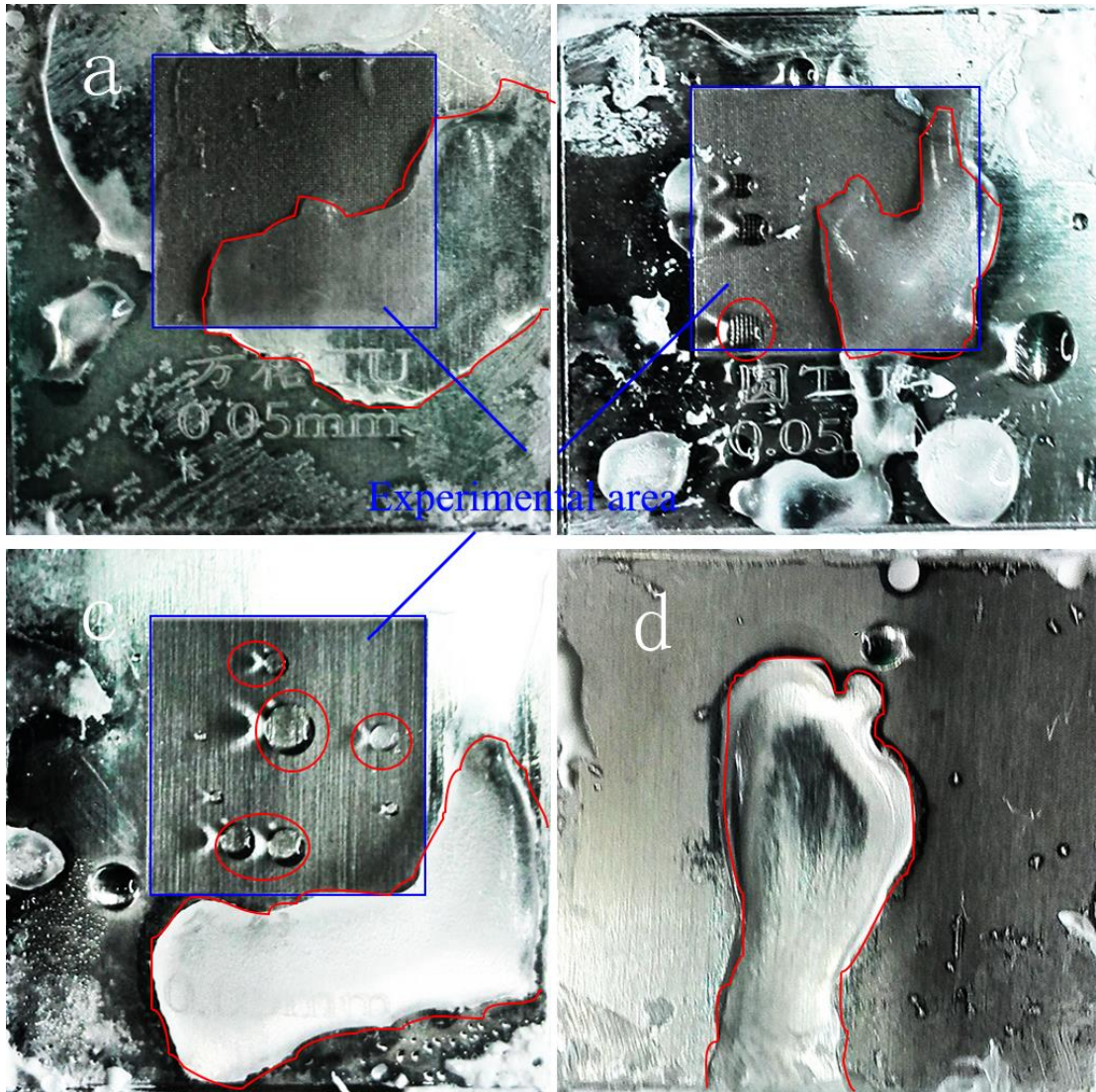
573 **Fig.5** WCA of different morphology of the as-prepared surface, bare  
 574 surface(B) ,square protuberance structure (S),round hump structure (R)  
 575 and mountain range-like structure (M),insets are optical images of the  
 576 static contact angle of 3  $\mu\text{L}$  water droplets. Insets are schematic  
 577 illustration of the wettability on the as-prepared surface with different  
 578 morphology; the triple-phase contact line of different superhydrophobic  
 579 surfaces is not identical, superhydrophobic surfaces with square  
 580 protuberance structure and round hump structure have larger contact area  
 581 than surfaces with mountain range-like structure.



582

583 **Fig.6** (1) In situ observation of ice formation on B-, R-, S-, and  
 584 M-surfaces at  $-15\text{ }^{\circ}\text{C}$  (a-d), (e) icing mechanism of water droplet on  
 585 as-prepared superhydrophobic surfaces. (2) Delayed freezing times of ice  
 586 formation on B-, R-, S- and M-surfaces at  $-15\text{ }^{\circ}\text{C}$ , and insets are the  
 587 status of water droplet at different time. (3) Model of heat transfer  
 588 process at the interface between the droplet and surface, (a)  
 589 superhydrophobic surface, (b) bare surface.

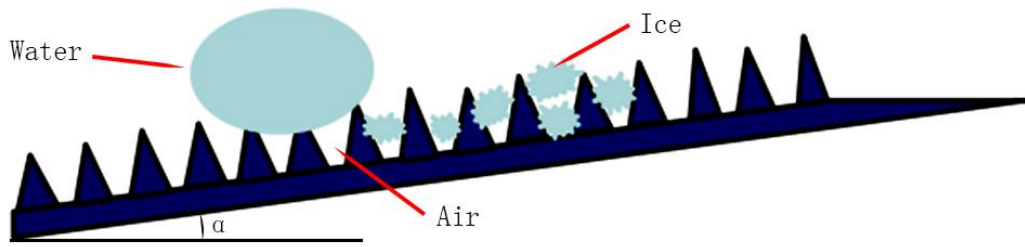




590

591 **Fig.7** The photographs of anti-icing test by spraying a stream of water  
 592 onto the as-prepared surfaces(a-d) square protuberance structure  
 593 (S),round hump structure (R) and mountain range-like structure (M) and  
 594 bare surface(B) respectively, the temperature of which was controlled at  
 595  $-15\text{ }^{\circ}\text{C}$  stably.

596



597

598 **Fig.8** Icing process model for dynamic situation. The micro water  
 599 droplets are easy to condensate in the gaps on the surface of  
 600 micro-structure at low temperature. As a result, most of the place used to  
 601 trap air is taken up by condensate water, so that the Cassie–Baxter state  
 602 disappears gradually. With the temperature of experimental plate  
 603 decreased further, parts of water could be peeled off and left on the  
 604 surface other than flow down, when the adhesive force is larger than Van  
 605 Der Waals force of the water.